Superconductivity in 122-type antimonide $BaPt_2Sb_2$

Motoharu Imai,[1] Soshi Ibuka,[1,*] Naoki Kikugawa,[1] Taichi Terashima,[2] Shinya Uji,[2] Takeshi Yajima,[3,4] Hiroshi Kageyama,[3] and Izumi Hase[5]

[1]*Superconducting Properties Unit, National Institute for Materials Science, 1-2-1 Sengen, Tsukuba, Ibaraki 305-0047, Japan*

[2]*Superconducting Properties Unit, National Institute for Materials Science, 3–13 Sakura, Tsukuba, Ibaraki 305-0003, Japan*

[3]*Graduate School of Engineering, Kyoto University, Nishikyo-ku, Kyoto 615–8510, Japan*

[4]*Institute for Solid State Physics, University of Tokyo, 5-1-5 Kashiwanoha, Kashiwa, Chiba 277–8581, Japan*

[5]*Electronics and Photonics Research Institute, National Institute of Advanced Industrial Science and Technology, AIST Central 2, 1-1-4 Umezono, Tsukuba, Ibaraki 305–8568, Japan*

(Received 22 September 2014; revised manuscript received 13 January 2015; published 30 January 2015)

The crystal structure, superconducting properties, and electronic structure of the novel superconducting 122-type antimonide $BaPt_2Sb_2$ have been studied by measurements of powder x-ray diffraction patterns, electrical resistivity, ac magnetic susceptibility, specific heat, and by *ab initio* calculations. The material crystallizes in a new monoclinic variant of the $CaBe_2Ge_2$-type structure, in which Pt_2Sb_2 layers that consist of $PtSb_4$ tetrahedra, and Sb_2Pt_2 layers that consist of $SbPt_4$ tetrahedra, are stacked alternatively, with Ba atoms located between them. Measurements of electrical resistivity, ac magnetic susceptibility, and specific heat revealed that $BaPt_2Sb_2$ is a superconducting material with a critical temperature of 1.8 K. The electronic heat capacity coefficient and the Debye temperature were 8.6 (2) $mJ/mol\,K^2$ and 146(4) K, respectively. The upper critical field and the Ginzburg-Landau coherent length were determined to be 0.27 T and 35 nm, respectively. The calculations showed that the material has two three-dimensional Fermi surfaces (FSs) and two two-dimensional FSs, leading to anisotropic transport properties. The *d* states of the Pt atoms in the Pt_2Sb_2 layers are the main contributors to the density of states at the Fermi level. A comparison between experimental and calculated results indicates that $BaPt_2Sb_2$ is a superconducting material with moderate coupling.

DOI: 10.1103/PhysRevB.91.014513 PACS number(s): 74.70.Xa, 74.25.−q, 74.20.Pq

I. INTRODUCTION

The discovery of superconductivity with a critical temperature T_C of 26 K in LaFeAs(O,F) [1] has stimulated studies on superconducting iron pnictides, and various systems such as 1111, 122, and 11 have been discovered [2–9]. AFe_2As_2 (A = Ba, Sr, Ca, or Eu) is the parent material for the superconducting 122 iron pnictides. Partial substitution of A, Fe, or As, or pressurization induces superconductivity with a relatively high T_C. For example, (Ba,K)Fe_2As_2 and (Ca, La)Fe_2(As, P)$_2$ have a T_C of 38 and 45 K, respectively [10,11]. AFe_2As_2 crystallizes with a $ThCr_2Si_2$-type structure, in which A atoms are located between Fe_2As_2 layers. Each Fe_2As_2 layer comprises a square lattice of Fe atoms, each of which is surrounded by four As atoms in a tetrahedral coordination.

Superconductivity has also been observed in iron-free pnictides with a $ThCr_2Si_2$-type or related structure, although their T_C values were relatively low [12–19]. $SrPt_2As_2$ is a superconductor with a T_C of 5.4 K [20]. It crystallizes in a modulated orthorhombic variant of the $CaBe_2Ge_2$-type structure, which is a derivative of the $ThCr_2Si_2$-type structure [21]. In $CaBe_2Ge_2$-type $SrPt_2As_2$, Sr atoms are sandwiched between two kinds of layers. One is a Pt_2As_2 layer, which is a similar structure to the Fe_2As_2 layer in AFe_2As_2. The other is an As_2Pt_2 layer, in which As atoms form a square lattice, with each being surrounded by four Pt atoms in a tetrahedral coordination. The electronic structure has been calculated for $ThCr_2Si_2$-type $SrPt_2As_2$, which is a hypothetical material, and $CaBe_2Ge_2$-type $SrPt_2As_2$ [22]. The results indicated that in the latter material, the Fermi surfaces (FSs) had characteristics that were intermediate between those for AFe_2As_2 and $ThCr_2Si_2$-phase iron-free pnictides. AFe_2As_2 has two-dimensional (2D) FSs [2,3,5,6,23,24], while $ThCr_2Si_2$-type iron-free pnictides have three-dimensional (3D) FSs [25–29]. $CaBe_2Ge_2$-type $SrPt_2As_2$ has two 2D FSs and two 3D FSs. The coexistence of 2D and 3D FSs has also been reported for $CaBe_2Ge_2$-type $BaPd_2Sb_2$ [29]. Thus, some $CaBe_2Ge_2$-type iron-free pnictides are positioned between $ThCr_2Si_2$-type iron pnictides and $ThCr_2Si_2$-type iron-free pnictides from the viewpoint of fermiology. Furthermore, the coexistence of 2D and 3D FSs is expected to cause multigap superconductivity, as in the case of MgB_2 [30,31], and this is an area of considerable interest in the field of superconductivity. Therefore, searching for superconducting $CaBe_2Ge_2$-type pnictides and studying their superconducting properties are important with regard to forming a systematic understanding of superconductivity in 122 pnictides.

However, superconducting materials that are structurally related to iron-based superconductors are limited to phosphides and arsensides. Recently, the 122 antimonide $SrPt_2Sb_2$ has been reported to be a superconductor with a T_C of 2.1 K [32]. To the best of our knowledge, this is the first report of a superconducting 122 antimonide that is related to superconducting iron pnictides. As previously reported, the crystal structure of $SrPt_2Sb_2$ is different to that of $CaBe_2Ge_2$ [21]. Although a precise analysis of the crystal structure needs to be performed, it is possibly related to the $CaBe_2Ge_2$-type structure. Since $SrPt_2Sb_2$ is isovalent to $SrPt_2As_2$ and deduced to have a crystal structure related to that of $CaBe_2Ge_2$, $SrPt_2Sb_2$

*Present address: Institute of Materials Structure Science, High Energy Accelerator Research Organization, 203-1 Shirakata, Tokai, Ibaraki 319–1106, Japan.

is expected to have both 3D and 2D FSs, and to exhibit physical properties that reflect this.

In this paper, we report on the successful synthesis of $BaPt_2Sb_2$, its crystal and electronic structures, and the appearance of superconductivity. To the best of our knowledge, $BaPt_2Sb_2$ is a novel material that has not so far been reported. A powder x-ray diffraction (XRD) analysis indicates that it crystallizes in a monoclinic variant of the $CaBe_2Ge_2$-type structure. Measurements of electrical resistivity, ac magnetic susceptibility, and specific heat reveal that $BaPt_2Sb_2$ is a superconducting material with a T_C of 1.82 K. *Ab initio* calculations demonstrate that it has 3D and 2D FSs, and that the main contribution to the density of states at the Fermi level $N(E_F)$, which is responsible for its superconductivity, is from the d states of Pt.

II. EXPERIMENTAL METHODS

The starting materials were Ba (purity 99.9%), Pt (purity 99.95%), and Sb (purity 99.999%). Samples were synthesized by Ar-arc melting of a 1.05:2:2 molar mixture of Ba, Pt, and Sb. Electron probe microanalysis (EPMA) revealed that the samples consisted of a matrix with a chemical composition of 20.2 at.% Ba, 40.6 at.% Pt, 39.3 at.% Sb, together with a small amount of Pt_xSb precipitates.

The crystal structure was examined by powder XRD using a Bragg-Brentano diffractometer (RINT-TTR III, Rigaku) with Cu $K\alpha$ radiation (40 kV, 300 mA), and a step size of 0.02° in the 2θ range of 15.0°–120.0° at room temperature. A fine powder sample was mounted on a glass plate holder with a depth of 0.3 mm. The XRD pattern was analyzed by the direct-space method with a simulated annealing algorithm, and subsequently refined by the Rietveld method [33] using the software "FULLPROF" [34]. The background was modeled using a six-coefficient polynomial function.

The electrical resistivity ρ at temperatures ranging from 1.8 to 300.0 K was measured by a four-probe method using a physical properties measurement system (PPMS, Quantum Design Co.). The magnetic field dependence of ρ was determined using a standard ac technique at a frequency (f) of ∼15 Hz.

The ac susceptibility $\chi_{ac} = \chi' - i\chi''$ was evaluated by a mutual-inductance method with an ac modulation field of $\mu_0 H_{ac} \sim 0.037$ mT and $f \sim 67$ Hz using the same sample used for the ac resistivity measurements. The sample was cooled using a dilution fridge that was equipped with a superconducting magnet for applying an external field. The specific heat was measured by a relaxation method using the PPMS.

In order to investigate the electronic structure of $BaPt_2Sb_2$, *ab initio* band calculations were performed for this compound. The full-potential linearized augmented plane-wave (FLAPW) scheme was used and the exchange-correlation potential was constructed within the local-density approximation. These were implemented using the KANSAI-94 and TSPACE [35] computer codes. The space group was $C2/m$ (No. 12), and the lattice constants and atomic parameters were set to experimentally observed values (this work). The muffin-tin radii used in this calculation were 2.6 bohrs for Ba, 2.4 bohrs for Pt, and 2.3 bohrs for Sb. For the plane-wave basis functions, about 1000 LAPWs were used. Since this compound contains the heavy atoms Pt and Sb, the spin-orbit interaction (SOI) was included using a second-variational approach [36]. In this scheme, a scalar-relativistic calculation was first performed, and the SOI was then included iteratively.

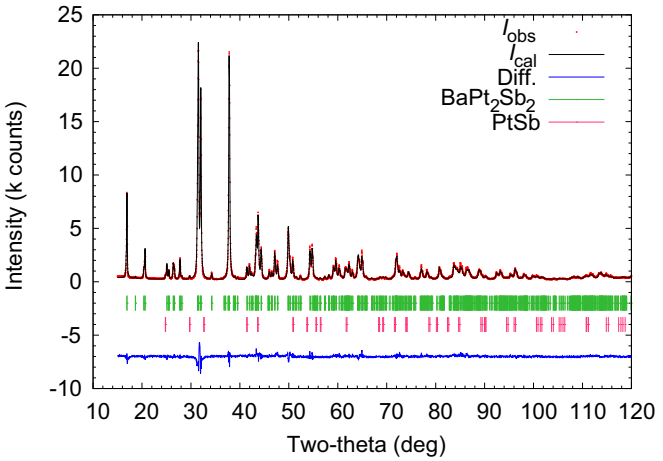

FIG. 1. (Color online) Powder XRD pattern for $BaPt_2Sb_2$. The red points and black line represent observed and calculated intensities, respectively. The difference between the two intensities is indicated by the blue line shifted by −7000 counts. Peak positions for $BaPt_2Sb_2$ and the PtSb impurity are labeled by green and purple vertical bars located at −2000 and −4000 counts, respectively.

III. RESULTS AND DISCUSSION

A. Crystal structure

Figure 1 shows a powder XRD pattern for $BaPt_2Sb_2$ together with the results of a Rietveld analysis. The observed pattern can be reproduced well by assuming that $BaPt_2Sb_2$ has a monoclinic structure with the parameters shown in Table I, and that a small amount (0.8 mol%) of a PtSb impurity phase is present. Figure 2 illustrates the crystal structure of $BaPt_2Sb_2$. The blue solid lines represent a unit cell. This is a new monoclinic variant of the $CaBe_2Ge_2$-type structure. In this structure, the Pt1 and Sb2 atoms form Pt_2Sb_2 layers that consist of $PtSb_4$ tetrahedra, while the Pt2 and Sb1 atoms form Sb_2Pt_2

TABLE I. Crystal structure of $BaPt_2Sb_2$. Monoclinic. Space group: $C2/m$ (No. 12). Lattice parameters: $a = 6.70156(10)$ Å, $b = 6.75246(10)$ Å, $c = 10.47440(14)$ Å, $\alpha_{uc} = 90.000°$, $\beta_{uc} = 91.2274(9)°$, $\gamma_{uc} = 90.000°$. $Z = 4$. $U_{iso} = 0.0057$ Å^2 (fixed). R factors: $R_p = 9.86$, $R_{wp} = 12.0$, $R_e = 4.57$, $\chi^2 = 6.939$. The definitions of R_p, R_{wp}, R_e, and χ^2 are in Ref. [33]. The values in parentheses represent the standard deviation.

Label	Atom	Multiplicity Wyckoff Position	x	y	z
Ba	Ba	4i	0.2549(6)	0.0000	0.7531(4)
Pt1	Pt	4g	0.0000	0.2823(3)	0.0000
Pt2	Pt	4i	0.2472(3)	0.0000	0.3791(2)
Sb1	Sb	4h	0.00000	0.2505(4)	0.50000
Sb2	Sb	4i	0.2276(5)	0.00000	0.1206(3)

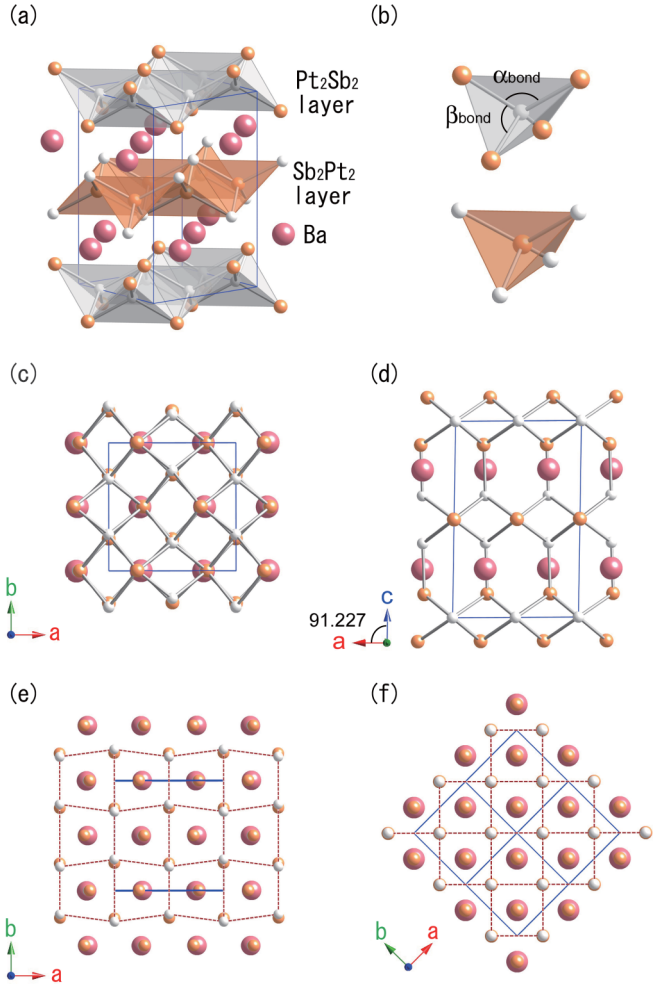

FIG. 2. (Color online) (a) Crystal structure of $BaPt_2Sb_2$, (b) $PtSb_4$ and $SbPt_4$ tetrahedra that form the Pt_2Sb_2 and Sb_2Pt_2 layers, (c) view along the [001] direction, (d) view along the [010] direction, (e) deformed Pt square lattice of $BaPt_2Sb_2$ along the [001] direction, and (f) Pt square lattice of $CaBe_2Ge_2$-type $BaPt_2Sb_2$ along the [001] direction. Red broken lines show Pt lattice. Blue solid lines show unit cell. Large purple spheres, small white spheres, and small orange spheres represent Ba, Pt, and Sb atoms, respectively.

layers that consist of $SbPt_4$ tetrahedra. These layers are stacked alternatively along the [001] direction, with Ba atoms between them. This crystal structure is similar to that for $CaBe_2Ge_2$, but some differences exist. First, the angle between the c axis and the a-b plane, β_{uc}, is 91.227°, whereas the three angles α_{uc}, β_{uc}, and γ_{uc}, are 90° in the $CaBe_2Ge_2$-type structure [Fig. 2(d)]. Second, the Pt1 (or Sb1) atoms form a deformed square lattice in the Pt_2Sb_2 (or Sb_2Pt_2) layers in the proposed structure, whereas Pt (or Sb) atoms form a square lattice in the Pt_2Sb_2 (or Sb_2Pt_2) layers in $CaBe_2Ge_2$-type $BaPt_2Sb_2$ (hypothetical) as shown in Figs. 2(e) and 2(f). The shape of the lattice formed by Pt1 (or Sb1) atoms is isosceles trapezoid, and the degree of deformation in the Pt1 lattice is larger than that for Sb1 atoms. The Pt1 (or Sb1) atoms are aligned along the b-axis direction, whereas they form a zigzag pattern along the a-axis direction. Third, the Pt1 (or Sb1) deformed square lattice in the proposed structure is almost parallel to the a and b axes, whereas the square lattice in the $CaBe_2Ge_2$-type structure is rotated 45° relative to the a and b axes [Figs. 2(e) and 2(f)].

A monoclinic variant of the $CaBe_2Ge_2$-type structure has been reported in materials such as $LnPt_2Ge_2$ (Ln = La − Dy) [37] and a high-pressure phase of $SrPt_2As_2$ [21], and this variant is known as the $LaPt_2Ge_2$-type structure. The $LaPt_2Ge_2$-type structure can be obtained from the $CaBe_2Ge_2$-type structure by changing the b-axis length and increasing the unit-cell angle β from 90° by several tenths of a degree. The relation between the unit-cell axis and the square Pt lattice is different for the $LaPt_2Ge_2$-type structure and the proposed crystal structure of $BaPt_2Sb_2$. In the $LaPt_2Ge_2$-type structure, the square lattice is rotated by 45° relative to the a and b axes, as in the case of the $CaBe_2Ge_2$-type structure, whereas the square lattice is almost parallel to the a and b axes in $BaPt_2Sb_2$. To the best of our knowledge, the proposed structure is a completely different one.

Table II lists interatomic distances. The intralayer interatomic distance has two values of 2.681(3) and 2.734(3) Å, which are both similar to the interlayer interatomic distance of 2.708(7) Å. This indicates that the crystal structure is three dimensional. The T_C for iron-based superconductors has often been discussed in terms of two structural parameters, the Pn-Fe-Pn angle in $FePn_4$ tetrahedra, and the Pn elevation above the Fe square lattice, where Pn represents pnictogen [38–40]. The Sb-Pt-Sb angles in the $PtSb_4$ tetrahedra and the Pt-Sb-Pt angles in the $SbPt_4$ tetrahedra are far from the ideal regular tetrahedron angle of 109.5° that is thought to be favorable for a high T_C in the iron pnictides. The Sb elevation above the distorted Pt square lattice is similar to the Pn elevation for iron pnictides with a high T_C.

The crystal structure of $SrPt_2Sb_2$ was reported to be different from the $CaBe_2Ge_2$-type [32], but has not been determined yet. This structure proposed in this paper may help to clarify the crystal structure of $SrPt_2Sb_2$.

TABLE II. Interatomic distances and bond angles. The values in parentheses represent the standard deviation.

Interatomic distances		
Intralayer		
Pt_2Sb_2 layer	2.681(3) Å × 2	2.734(3) Å × 2
	Sb height from the Pt square lattice	1.263(3) Å
Sb_2Pt_2 layer	2.687(2) Å × 2	2.702(2) Å × 2
	Pt height from the Sb square lattice	1.266(2) Å
Interlayer	2.708(7) Å	
Bond angles		
$PtSb_4$ tetrahedron		
Sb-Pt-Sb angle		
Diagonal (α_{bond})	122.92(15)° × 2	
Adjacent (β_{bond})	91.58(16)°, 102.78(12)° × 2, 113.50(19)°	
$SbPt_4$ tetrahedron		
Pt-Sb-Pt angle		
Diagonal (α_{bond})	123.95(12)° × 2	
Adjacent (β_{bond})	102.47(12)°, 103.10(9)° × 2, 102.34(12)°	

B. Electrical resistivity, ac magnetic susceptibility, specific heat, and magnetic phase diagram

Based on the results of electrical resistivity, ac magnetic susceptibility, and specific-heat measurements, it was found that $BaPt_2Sb_2$ undergoes a superconducting transition.

Figure 3(a) shows the electrical resistivity ρ as a function of temperature, where the inset is an expanded view at low temperatures. It can be seen that ρ decreases with decreasing temperature, undergoes an abrupt drop at 1.85 K, and becomes negligibly small at 1.82 K, which suggests that $BaPt_2Sb_2$ undergoes a normal-to-superconducting transition. The residual resistivity ratio $\rho\,(300\,\mathrm{K})\,/\rho\,(2\,\mathrm{K})$ is 4.04. Figure 3(b) shows ρ measured at constant temperatures as a function of the magnetic field strength. Under an applied magnetic field, the sample underwent a superconducting-to-normal transition. The symbols $H_{C2}{}^{\rho\text{-on}}$, $H_{C2}{}^{\rho\text{-mid}}$, and $H_{C2}{}^{\rho\text{-comp}}$ represent the magnetic field strength at which ρ starts to increase from zero, that where ρ is half the normal resistivity value, and that where an extrapolation of the ρ-T curve at the transition reaches the normal resistivity value, respectively. The critical field increases with decreasing temperature, as will be discussed in more detail later.

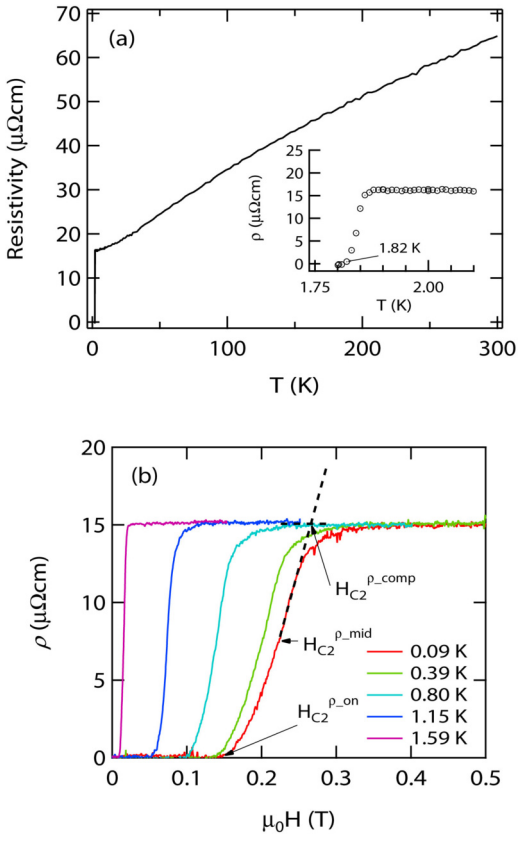

FIG. 3. (Color online) (a) Electrical resistivity as a function of temperature, (b) electrical resistivity at fixed temperatures as a function of magnetic field strength. The inset in Fig. 3(a) is an expanded view of the resistivity at low temperatures ranging from 1.8 to 2.1 K. The symbols $H_{C2}{}^{\rho\text{-on}}$, $H_{C2}{}^{\rho\text{-mid}}$, and $H_{C2}{}^{\rho\text{-comp}}$ represent the magnetic field strength at which ρ starts to increase from zero, that at which ρ is half the normal resistivity value, and that at which an extrapolation of the ρ-T curve during the transition reaches the normal resistivity value, respectively.

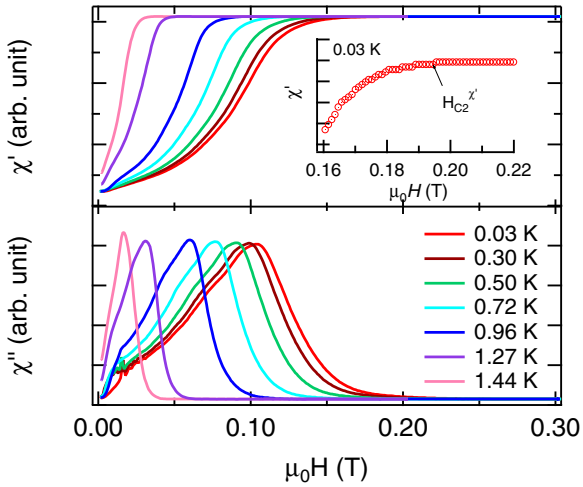

FIG. 4. (Color online) Real and imaginary parts of ac magnetic susceptibility χ' and χ'', respectively, measured at constant temperatures below 1.44 K as a function of magnetic field amplitude $\mu_0 H$. The inset shows an expanded view of χ' measured at 0.03 K. $H_{C2}{}^{\chi'}$ indicates the magnetic field amplitude where the diamagnetic signal disappears.

Figure 4 shows the real and imaginary parts of the ac magnetic susceptibility χ' and χ'', respectively, measured at constant temperatures below 1.44 K as a function of magnetic field amplitude $\mu_0 H$. The inset is an expanded view of χ' measured at 0.03 K. The χ' curves reflect a diamagnetic signal at low $\mu_0 H$, and this disappears at the point $\mu_0 H_{C2}{}^{\chi'}$. The χ'' curves exhibit a peak at a magnetic field amplitude almost corresponding to the inflection point in the χ' curves. The shoulder observed at low $\mu_0 H$ in the χ'' curves is due to a background signal associated with the apparatus. This behavior of χ' and χ'' suggests that $BaPt_2Sb_2$ becomes superconducting in this temperature range [41], and that the abrupt decrease in ρ at 1.85 K corresponds to a superconducting transition. The magnitude of the diamagnetic signal for $BaPt_2Sb_2$ was investigated by comparing it with that for a Pb sample with the same shape and size. At 1.6 K, the two signals had almost the same magnitude, and since Pb is a perfect diamagnet at this temperature, the superconducting volume fraction in $BaPt_2Sb_2$ was almost 100%.

Figure 5(a) shows the specific heat divided by the temperature C/T as a function of T^2, measured for different magnetic field strengths. At 0 T, an anomaly appears around 1.7 K, and this shifts to lower temperature and becomes smaller with increasing magnetic field, until it finally disappears at 0.2 T. This large specific-heat anomaly and the large diamagnetic signal in χ' indicate that the observed superconductivity is bulk superconductivity. These results reveal that $BaPt_2Sb_2$ is a superconducting material with a T_C of 1.8 K.

The electronic specific-heat coefficient γ_n, and the coefficients β and δ were determined to be 8.6 (2) mJ/mol K^2, 2.32 (6) mJ/mol K^4, and 0.111 (5) mJ/mol K^6, respectively, by fitting the equation $C/T = \gamma_n + \beta T^2 + \delta T^4$ to the data obtained at 0.2 T. The Debye temperature θ_D was calculated to be 146(4) K from the value of β. In order to confirm the validity of the fit, the difference in the entropy S between the normal and superconducting states $S_{es} - S_{en}$ was calculated

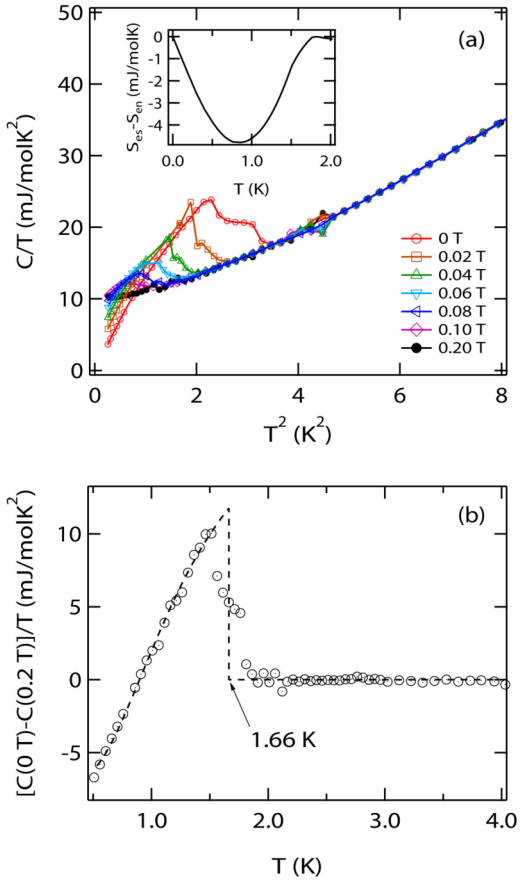

FIG. 5. (Color online) (a) Specific heat divided by temperature C/T, measured at various magnetic field strengths as a function of squared temperature T^2, and (b) specific-heat difference between 0 and 0.2 T divided by temperature $[C\,(0\,\mathrm{T}) - C\,(0.2\,\mathrm{T})]/T$ as a function of temperature. The inset in Fig. 5(a) shows the difference in entropy S between the normal and superconducting states $S_{\mathrm{es}} - S_{\mathrm{en}}$ as a function of temperature.

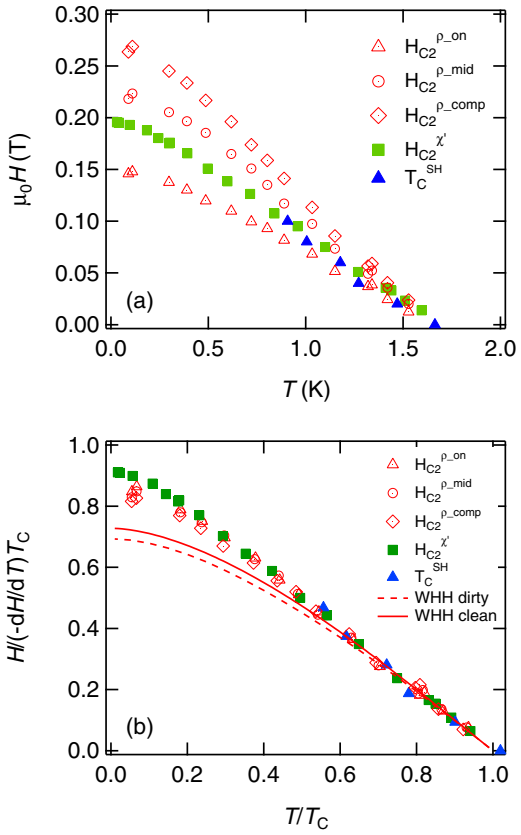

FIG. 6. (Color online) (a) Magnetic field-temperature phase diagram deduced from measurements of electrical resistivity, ac magnetic susceptibility, and specific heat. The empty triangles, circles, and rhombus indicate $T_{\mathrm{C}}{}^{\rho\text{-on}}$, $T_{\mathrm{C}}{}^{\rho\text{-mid}}$, and $T_{\mathrm{C}}{}^{\rho\text{-comp}}$, shown in Fig. 3(b). The solid squares and triangles represent H_{C2} determined from χ', and T_{C} determined from the specific-heat data, respectively. (b) Reduced magnetic field h^* as a function of reduced temperature t^*, where $h^* = H/(-dH/dT)T_{\mathrm{C}}$ and $t^* = T/T_{\mathrm{C}}$. The dashed-dotted and dotted lines show h^* calculated using a pair-breaking model in the clean and dirty limits, respectively.

by integrating $(C_{\mathrm{es}} - \gamma_{\mathrm{n}})/T$ between 0 and 2 K, where C_{es} is the electronic specific heat for the superconducting state. C_{es} is obtained by subtracting the phonon specific heat $C_{\mathrm{ph}} = \beta T^3 + \delta T^5$ from C (0 T) and extrapolating C_{es} (0 T) to 0 K. The entropy difference goes to zero when the temperature reaches 1.8 K, as shown in the inset, which confirms the thermodynamic consistency of the fit.

In Fig. 5(b), the difference in C/T between 0 and 0.2 T, $[C\,(0\,\mathrm{T}) - C\,(0.2\,\mathrm{T})]/T$, is shown as a function of the temperature. The dashed line represents an entropy-conserving construction. The transition to the superconducting state with the entropy-conserving construction gives $\Delta C\,(T_{\mathrm{C}})/T_{\mathrm{C}} = 11.8(2)\,\mathrm{mJ/mol\,K^2}$ and $T_{\mathrm{C}} = 1.66$ K. The ratio of the specific-heat jump at T_{C} to γ_{n}, $\Delta C\,(T_{\mathrm{C}})/\gamma_{\mathrm{n}}\,T_{\mathrm{C}}$, is calculated to be 1.37, which is almost the same as that predicted by BCS theory (1.43) [42].

The anomaly in the $C/T - T$ curve has a shoulder at 1.76 K. A detailed investigation of the shoulder region is currently underway. However, it is possibly the result of multigap superconductivity or spatial inhomogeneity in the chemical composition of the samples.

Figure 6(a) is a magnetic field-temperature phase diagram deduced from the measurements of electrical resistivity, ac magnetic susceptibility, and specific heat. The empty triangles, circles, and rhombus represent $T_{\mathrm{C}}{}^{\mathrm{r\text{-}on}}$, $T_{\mathrm{C}}{}^{\rho\text{-mid}}$, and $T_{\mathrm{C}}{}^{\rho\text{-comp}}$ shown in Fig. 3(b), respectively. The solid squares represent $H_{\mathrm{C2}}{}^{\chi'}$, as shown in the inset of Fig. 4. The solid triangles represent the superconducting critical temperature $T_{\mathrm{C}}{}^{\mathrm{SH}}$ determined from the specific-heat data using the entropy-conserving construction.

Figure 6(b) shows the reduced magnetic field h^* as a function of the reduced temperature t^*, where $h^* = H/(-dH/dT)T_{\mathrm{C}}$ and $t^* = T/T_{\mathrm{C}}$. The dashed-dotted and dotted lines show h^* calculated using the pair-breaking model proposed by Werthamer, Helfand, and Hohenber (WHH), in the clean and dirty limits [43–45], respectively. The $h^* - t^*$ curve obtained from the resistivity data agrees with those obtained from the ac magnetic susceptibility and specific-heat data. The t^* dependence of h^* deviates from the calculated curve. The value of $H_{\mathrm{C2}}\,(0)$ was therefore determined to be 0.27 T from $\mu_0 H_{\mathrm{C2}}{}^{\rho\text{-comp}}$. This value is approximately one-tenth of the Pauli limiting field $\mu_0 H_{\mathrm{P}}$ (3.31 T), defined as

$H_P = 18.4T_C$ (kOe) [46,47], which indicates the absence of Pauli limiting in $BaPt_2Sb_2$. The Ginzburg-Landau (GL) coherent length ξ (0) was determined to be 35 nm using the formula $H_{C2}(0) = \Phi_0/2\pi\xi(0)^2$, where Φ_0 is the flux quantum [42].

As described above, the t^* dependence of h^* deviates from the calculated curve based on the pair-breaking model proposed by WHH, assuming that the superconductor has a single superconducting gap. A similar deviation has been observed for iron pnictides such as $LaFeAsO_{1-x}F_x$ [48], Co-doped $SrFe_2As_2$ [49], and Co-doped $BaFe_2As_2$ [50], and was interpreted within the framework of a two-gap model. A theory for two-gap superconductors indicated that the $T - H_{C2}(T)$ curve can differ from that predicted by single-gap theory, and that $H_{C2}(0)$ can considerably exceed the value determined based on the one-gap model in the dirty limit, $0.7T_C dH_{C2}/dT_C$ [51]. In the case of MgB_2, two superconducting gaps are formed as a result of a 2D cylindrical FS and a 3D tubular-network FS [31,32]. $BaPt_2Sb_2$ has four FS sheets with different dimensionality and carrier type. Two are 2D electronlike FSs and two are 3D holelike FSs, as later calculations will show. Therefore, these FSs are expected to form multiple superconducting gaps in $BaPt_2Sb_2$, as in the case of MgB_2. Therefore, the observed deviation in the $t^* - h^*$ curve might be due to such multigap superconductivity. Further study using single-crystalline samples is necessary in order to confirm whether the presence of multiple gaps plays an important role in the superconductivity of $BaPt_2Sb_2$.

C. Electronic structure

Figures 7 and 8 illustrate the band structure and the total and partial density of states (DOS) for $BaPt_2Sb_2$. The bands in the energy range from −0.2 to 0.0 Ry mainly consists of Sb *s*-states. The bands in the energy range from 0.1 to 0.7 Ry mainly consist of Sb *p* and Pt *d* states. Above 0.7 Ry, the bands originate from the Ba *d* and Pt *d* states. Since the bands associated with Pt and Sb are broad, the correlation is deduced

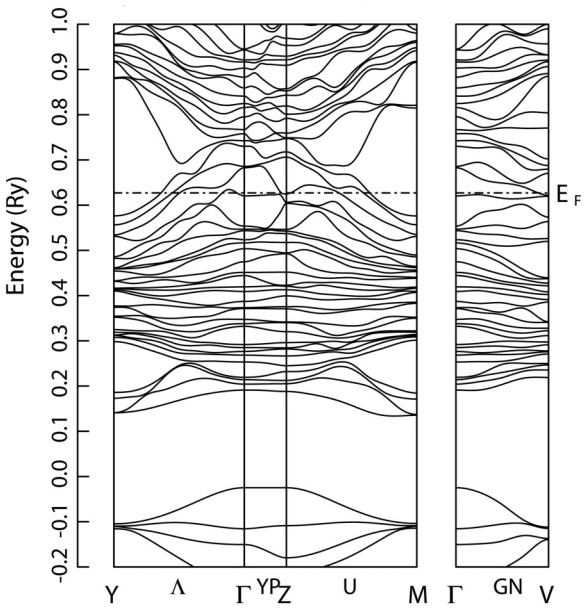

FIG. 7. Band structure of $BaPt_2Sb_2$.

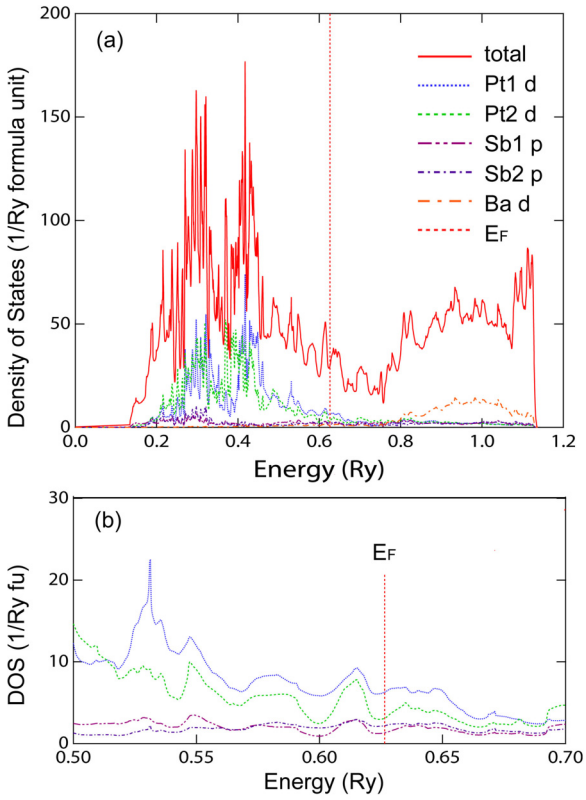

FIG. 8. (Color online) (a) Total and partial density of states (DOS) for $BaPt_2Sb_2$. (b) Expanded view of partial DOS for $BaPt_2Sb_2$ near the Fermi level E_F.

to be weak in $BaPt_2Sb_2$. Four bands cross the Fermi level E_F, as can be seen clearly on the Γ-*Y* line. $N(E_F)$ is 29.8 states/Ry/chemical formula unit, or 2.58 states/eV/chemical formula unit. Figure 8(b) shows an expanded view of the partial DOS near E_F. $N(E_F)$ mainly consists of Sb *p* and Pt *d* states, and the contribution from the Pt *d* states is larger, particularly for Pt1 atoms (Pt atoms at 4*g* site in Table I). The contributions of the Pt2 *d*, Sb2 *p*, and Sb1 *p* states are approximately one half, one third, and one fifth of that of the Pt1 *d* states, respectively. It is worth noting that the Pt1 atoms are in $PtSb_4$ tetrahedra in the Pt_2Sb_2 layers. These results suggest that carrier conduction mainly occurs in these layers.

The four bands that cross E_F on the Γ-*Y* line from the Γ to *Y* points are the 37th, 38th, 39th, and 40th bands from the bottom, respectively, which results in four FS sheets, as illustrated in Fig. 9. The sheets formed by the 37th and 38th bands are holelike, whereas the other two are electronlike. The 37th and 38th bands form 3D FSs around the Γ point. The 39th and 40th bands form 2D FSs with a cylindrical shape along the k_z direction at the corners near the *M* point.

The shape of the FSs in $BaPt_2Sb_2$ is similar to that observed in $BaPd_2Sb_2$ [29] and $SrPt_2As_2$ [22] in that there are two 3D FSs and two 2D FSs. However, the carrier types are different. $SrPt_2As_2$ has one holelike FS and three electronlike FSs, whereas $BaPt_2Sb_2$ has two holelike FSs and two electronlike FSs, as in the case of $BaPd_2Sb_2$.

The anisotropic shape of the FSs is expected to be reflected in anisotropic transport properties. To investigate this, the Fermi velocity components $v_F{}^x$ and $v_F{}^z$ were calculated

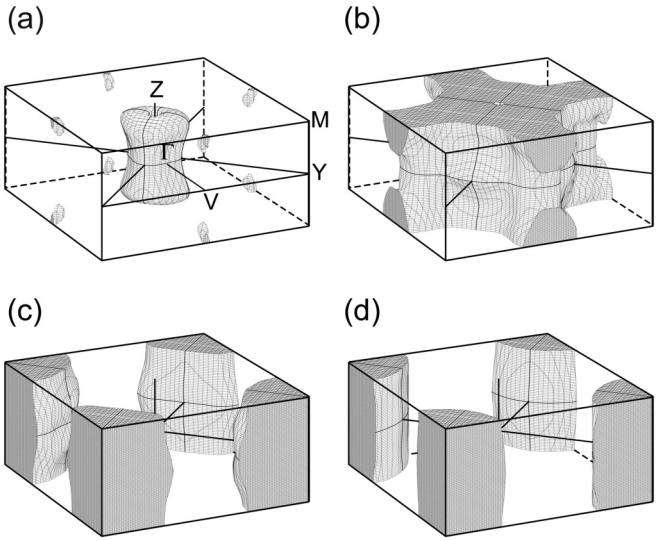

FIG. 9. Fermi surfaces (FSs) for $BaPt_2Sb_2$, formed by the (a) 37th, (b) 38th, (c) 39th, and (d) 40th bands. The FSs for the 37th and 38th bands are holelike, and FSs for the 39th and 40th bands are electronlike.

assuming the angle β_{uc} in the unit cell to be 90° because the first two digits in the Fermi velocities are the same for crystal structures with β_{uc} values of 90° and 91.227°. Table III lists the average values of $v_F{}^x$ and $v_F{}^z$, and the ratio $v_F{}^x/v_F{}^z$ for $BaPt_2Sb_2$ together with the two polymorphs $BaPd_2Sb_2$ and $SrPt_2As_2$. The $v_F{}^x/v_F{}^z$ values are clearly greater than unity for $BaPt_2Sb_2$ and the $CaBe_2Ge_2$-type materials, which suggests that these materials have anisotropic transport properties. On the other hand, those for the $ThCr_2Si_2$-type materials are close to unity, suggesting isotropic transport properties. Thus, the existence of 2D FSs in $BaPt_2Sb_2$ and the $CaBe_2Ge_2$-type materials is reflected in anisotropic transport properties.

Table IV lists T_C, γ_n, θ_D, $N(E_F)$, and the electron-phonon coupling constant λ for $BaPt_2Sb_2$, $SrPt_2Sb_2$ [32], $LaPd_2Sb_2$ [52], and $SrPt_2As_2$ [20,22]. $LaPd_2Sb_2$ is a recently reported superconducting material ($T_C = 1.4$ K) with the $CaBe_2Ge_2$-type structure. $\gamma_n{}^{expt}$ is γ_n obtained from specific-heat measurements and $\gamma_n{}^{calc}$ is γ_n calculated using the equation $\gamma_n{}^{calc} = (\pi^2/3)N(E_F)k_B{}^2.\lambda$ was estimated to be 0.67 for $BaPt_2Sb_2$ using the relation $\gamma_n{}^{expt} = (1+\lambda)\gamma_n{}^{calc}$. $BaPt_2Sb_2$ is a superconducting material with moderate coupling. The value of $\gamma_n{}^{expt}$ for $BaPt_2Sb_2$ is comparable to those for $SrPt_2Sb_2$ and $SrPt_2Sb_2$, and is slightly larger than that for $LaPd_2Sb_2$. θ_D for $BaPt_2Sb_2$ is the smallest among the four compounds. The value of λ is comparable to that for $SrPt_2As_2$.

TABLE III. Average Fermi velocity components $v_F{}^x$ and $v_F{}^z$, and the ratio $v_F{}^x/v_F{}^z$ for $BaPt_2Sb_2$ and the $CaBe_2Ge_2$- and $ThCr_2Si_2$-type polymorphs of $BaPd_2Sb_2$ [29] and $SrPt_2As_2$ [22].

Materials	$v_F{}^x$ (10^7 cm/s)	$v_F{}^z$ (10^7 cm/s)	$v_F{}^x/v_F{}^z$
$BaPt_2Sb_2$	4.4	2.1	2.1
$CaBe_2Ge_2$ type			
$BaPd_2Sb_2$			2.9[a]
$SrPt_2As_2$	2.47[b]	1.62[b]	1.52[b]
$ThCr_2Si_2$ type			
$BaPd_2Sb_2$			0.72[a]
$SrPt_2As_2$	1.93[b]	1.87[b]	1.03[b]

[a]Reference [29].
[b]Reference [22].

IV. CONCLUSION

This study clearly demonstrated that the 122-type antimonide, $BaPt_2Sb_2$, which is structurally related to the iron-based superconductors, shows superconductivity with a T_C of 1.8 K. $BaPt_2Sb_2$ crystallizes in a new monoclinic variant of the $CaBe_2Ge_2$-type structure. Calculations showed that it has two 3D FSs and two 2D FSs, which results in anisotropic transport properties. The d states of Pt atoms in $PtSb_4$ tetrahedra in the Pt_2Sb_2 layers make the main contribution to $N(E_F)$. A comparison between experimental and calculation results indicated that $BaPt_2Sb_2$ is a superconducting material with moderate coupling.

This study also demonstrated that unknown variants of the $CaBe_2Ge_2$-type structure may exist in 122-type pnictides. It is therefore worthwhile to search for superconducting 122 antimonides with a $CaBe_2Ge_2$-type structure or variant since this can lead to the discovery of new superconducting materials. Since the calculated electronic structure for $CaBe_2Ge_2$-type iron-free pnictides indicates that they have characteristics intermediate between those for $ThCr_2Si_2$-type iron and iron-free pnictides, this will also aid in forming a systematic understanding of superconductivity in 122 pnictides.

TABLE IV. Superconducting critical temperature T_C, electronic heat capacity coefficient γ_n, Debye temperature θ_D, calculated density of states at the Fermi level $N(E_F)$, and electron-phonon coupling constant λ for $BaPt_2Sb_2$, $SrPt_2Sb_2$ [32], $LaPd_2Sb_2$ [52], and $SrPt_2As_2$ [20,22]. $\gamma_n{}^{expt}$ is γ_n obtained from specific-heat measurements, and $\gamma_n{}^{calc}$ is γ_n estimated by calculations. The values in parentheses represent the standard deviation.

	T_C (K)	$\gamma_n{}^{expt}$ (mJ/mol K^2)	θ_D (K)	$N(E_F)$ (states/eV cell)	$\gamma_n{}^{calc}$ (mJ/mol K^2)	λ
$BaPt_2Sb_2$	1.82	8.6(2)	146(4)	2.19	5.16	0.67
$SrPt_2Sb_2$	2.1[a]	9.2(1)[a]	183[a]			–
$LaPd_2Sb_2$	1.4[b]	6.89[b]	210[b]			
$SrPt_2As_2$	5.2[c]	9.72[c]	211[c]	2.55[d]	6.01[d]	0.62[d]

[a]Reference [32].
[b]Reference [52].
[c]Reference [20].
[d]Reference [22].

ACKNOWLEDGMENTS

The authors thank M. Nishio of National Institute for Materials Science (NIMS) for EPMA, M. Takagi of NIMS for experimental support, Y. Yamada, F. Ishikawa, and N. Eguchi of Niigata University for their support at the first stage of the synthesis. This work was supported in part by the Japan Society for the Promotion of Science through its "Funding Program for World-Leading Innovative R&D on Science and Technology (FIRST Program)."

[1] Y. Kamihara, T. Watanabe, M. Hirano, and H. Hosono, J. Am. Chem. Soc. **130**, 3296 (2008).
[2] N.-L. Wang, H. Hosono, and P. Dai, *Iron-Based Superconductors* (Pan Stanford Publishing, Singapore, 2013).
[3] Y. Izyumov and E. Kurmaev, *High-T_C Supercpnductors Based on FeAs Compounds* (Springer, Heidelberg, 2010).
[4] H. Hosono, J. Phys. Soc. Jpn. **77**, 1 (2008).
[5] D. C. Johnston, Adv. Phys. **59**, 803 (2010).
[6] J. Paglione and R. L. Greene, Nat. Phys. **6**, 645 (2010).
[7] P. J. Hirschfeld, M. M. Korshunov, and I. I. Mazin, Rep. Prog. Phys. **74**, 124508 (2011).
[8] G. R. Stewart, Rev. Mod. Phys. **83**, 1589 (2011).
[9] K. Ishida, Y. Nakai, and H. Hosono, J. Phys. Soc. Jpn. **78**, 062001 (2009).
[10] M. Rotter, M. Tegel, and D. Johrendt, Phys. Rev. Lett. **101**, 107006 (2008).
[11] K. Kudo, K. Iba, M. Takasuga, Y. Kitahama, J. Matsumura, M. Danura, Y. Nogami, and M. Nohara, Sci. Rep. **3**, 1478 (2013).
[12] F. Ronning, E. D. Bauer, T. Park, S. H. Baek, H. Sakai, and J. D. Thompson, Phys. Rev. B **79**, 134507 (2009).
[13] T. Mine, H. Yanagi, T. Kamiya, Y. Karnihara, M. Hirano, and H. Hosono, Solid State Commun. **147**, 111 (2008).
[14] D. Hirai, T. Takayama, R. Higashinaka, H. Aruga-Katori, and H. Takagi, J. Phys. Soc. Jpn. **78**, 023706 (2009).
[15] W. Jeitschko, R. Glaum, and L. Boonk, J. Solid State Chem. **69**, 93 (1987).
[16] J.-T. Han, J.-S. Zhou, J.-G. Cheng, and J. B. Goodenough, J. Am. Chem. Soc. **132**, 908 (2010).
[17] E. D. Bauer, F. Ronning, B. L. Scott, and J. D. Thompson, Phys. Rev. B **78**, 172504 (2008).
[18] D. Hirai, T. Takayama, D. Hashizume, R. Higashinaka, A. Yamamoto, A. K. Hiroko, and H. Takagi, Physica C (Amsterdam) **470**, S296 (2010).
[19] F. Ronning, N. Kurita, E. D. Bauer, B. L. Scott, T. Park, T. Klimczuk, R. Movshovich, and J. D. Thompson, J. Phys.: Condens. Matter **20**, 342203 (2008).
[20] K. Kudo, Y. Nishikubo, and M. Nohara, J. Phys. Soc. Jpn. **79**, 123710 (2010).
[21] A. Imre, A. Hellmann, G. Wenski, J. Grap, D. Johrendt, and A. Mewis, Z. Anorg. Allg. Chem. **633**, 2037 (2007).
[22] I. R. Shein and A. L. Ivanovskii, Phys. Rev. B **83**, 104501 (2011).
[23] D. J. Singh, Phys. Rev. B **78**, 094511 (2008).
[24] C. Liu, G. D. Samolyuk, Y. Lee, N. Ni, T. Kondo, A. F. Santander-Syro, S. L. Bud'ko, J. L. McChesney, E. Rotenberg, T. Valla, A. V. Fedorov, P. C. Canfield, B. N. Harmon, and A. Kaminski, Phys. Rev. Lett. **101**, 177005 (2008).
[25] A. Subedi and D. J. Singh, Phys. Rev. B **78**, 132511 (2008).
[26] I. R. Shein and A. L. Ivanovskii, Phys. Rev. B **79**, 054510 (2009).
[27] I. R. Shein and A. L. Ivanovskii, Solid State Commun. **149**, 1860 (2009).
[28] I. R. Shein and A. L. Ivanovskii, Physica B (Amsterdam) **405**, 3213 (2010).
[29] I. Hase and T. Yanagisawa, Physica C (Amsterdam) **494**, 27 (2013).
[30] H. J. Choi, D. Roundy, H. Sun, M. L. Cohen, and S. G. Louie, Nature (London) **418**, 758 (2002).
[31] A. Y. Liu, I. I. Mazin, and J. Kortus, Phys. Rev. Lett. **87**, 087005 (2001).
[32] M. Imai, S. Emura, M. Nishio, Y. Matsushita, S. Ibuka, N. Eguchi, F. Ishikawa, Y. Yamada, T. Muranaka and J. Akimitsu, Supercond. Sci. Technol. **26**, 075001 (2013).
[33] R. A. Young, *The Rietveld Method* (Oxford University Press, Oxford, 1993).
[34] J. Rodriguezcarvajal, Physica B (Amsterdam) **192**, 55 (1993).
[35] A. Yanase, *Fortran Program For Space Group (TSPACE)* (Shokabo, Tokyo, 1995).
[36] D. D. Koelling and B. N. Harmon, J. Phys. C: Solid State Phys. **10**, 3107 (1977).
[37] G. Venturini, B. Malaman, and B. Roques, J. Less-Common Met. **146**, 271 (1989).
[38] C. H. Lee, A. Iyo, H. Eisaki, H. Kito, M. T. Fernandez-Diaz, T. Ito, K. Kihou, H. Matsuhata, M. Braden, and K. Yamada, J. Phys. Soc. Jpn. **77**, 083704 (2008).
[39] D. Johrendt, H. Hosono, R. D. Hoffmann, and R. Pottgen, Z. Kristallogr. **226**, 435 (2011).
[40] K. Kuroki, H. Usui, S. Onari, R. Arita, and H. Aoki, Phys. Rev. B **79**, 224511 (2009).
[41] A. F. Khoder, Phys. Lett. A **94**, 378 (1983).
[42] M. Tinkham, *Introduction to Superconductivity*, 2nd ed. (McGraw-Hill, New York, 1996).
[43] E. Helfand and N. R. Werthamer, Phys. Rev. Lett. **13**, 686 (1964).
[44] E. Helfand and N. R. Werthamer, Phys. Rev. **147**, 288 (1966).
[45] N. Werthame, E. Helfand, and P. Hohenber, Phys. Rev. **147**, 295 (1966).
[46] B. S. Chandrasekhar, Appl. Phys. Lett. **1**, 7 (1962).
[47] A. M. Clogston, Phys. Rev. Lett. **9**, 266 (1962).
[48] F. Hunte, J. Jaroszynski, A. Gurevich, D. C. Larbalestier, R. Jin, A. S. Sefat, M. A. McGuire, B. C. Sales, D. K. Christen, and D. Mandrus, Nature (London) **453**, 903 (2008).
[49] S. A. Baily, Y. Kohama, H. Hiramatsu, B. Maiorov, F. F. Balakirev, M. Hirano, and H. Hosono, Phys. Rev. Lett. **102**, 117004 (2009).
[50] M. Kano, Y. Kohama, D. Graf, F. Balakirev, A. S. Sefat, M. A. McGuire, B. C. Sales, D. Mandrus, and S. W. Tozer, J. Phys. Soc. Jpn. **78**, 084719 (2009).
[51] A. Gurevich, Phys. Rev. B **67**, 184515 (2003).
[52] S. Ganesanpotti, T. Yajima, T. Tohyama, Z. Li, K. Nakano, Y. Nozaki, C. Tassel, Y. Kobayashi, and H. Kageyama, J. Alloys Compd. **583**, 151 (2014).